

Pseudorandom phase-only encoding of real-time spatial light modulators

Robert W. Cohn and Minhua Liang

We previously proposed a method of mapping full-complex spatial modulations into phase-only modulations. The Fourier transform of the encoded modulations approximates that of the original complex modulations. The amplitude of each pixel is encoded by the property that the amplitude of a random-phaser sum is reduced corresponding to its standard deviation. Pseudorandom encoding is designed for phase-only spatial light modulators that produce 360° phase shifts. Because such devices are rare, experiments are performed with a 326° modulator composed of two In Focus model TVT6000 liquid-crystal displays. Qualitative agreement with theory is achieved despite several nonideal properties of the modulator.

Key words: Optical information processing, spatial light modulators, liquid-crystal televisions, phase-only filters, laser speckle, rough-surface scattering, statistical optics, binary and diffractive optics, phased arrays, measurements of phase. © 1996 Optical Society of America

1. Introduction

Pseudorandom phase-only encoding¹ is a method for designing phase-only filters and diffractive optical elements that approximately produces the same Fraunhofer diffraction pattern as would result from a desired, but unrealizable, full-complex filter. The encoding procedure adds amplitude control to the phase-only filter² through the addition of phase offsets that have specified statistical properties. The randomness of the phase offset at a given pixel, as measured by the standard deviation of this random variable, determines the effective attenuation caused by the pixel insofar as it describes its effect on the Fraunhofer pattern. Each pixel can be programmed in this way to have a specified value of phase and effective amplitude. The fact that the resulting diffraction pattern approximates the desired diffraction pattern from the full-complex modulation is a result of the law of large numbers. In this situation the individual Huygens wave fronts from all spatially separated pixels in the modulator plane all coincide and coherently add together across the Fraunhofer plane (as illustrated in Fig. 1). If

the amount of randomness present in the input pixels is not too large, then a coherent reconstruction is observed that approximates the diffraction pattern from the full-complex modulation. If the randomness is too great, only a speckle pattern is observed. We also show that the quality of the reconstruction, in terms of how well it approximates the desired diffraction pattern, is closely related to the average intensity transmittance of the desired full-complex modulation. Because this metric is calculated directly from the full-complex modulation, it can be used in advance of performing the encoding to determine whether or not the phase-only modulation provides adequate performance for the given application.

The method is especially well suited for real-time programming of spatial light modulators (SLM's). The mapping, because it requires one function calculation (or table lookup) per pixel, can be computed at the frame rate by a serial electronic processor. This is in contrast to many diffractive-optic and filter-design procedures that focus on optimal synthesis of a desired diffraction pattern under the constraint of phase-only modulation. These latter approaches are appropriate for the design of fixed-pattern filters; however, as they are numerically intensive, they usually cannot be performed in real time. For some applications it may be adequate to precompute the mapping off-line, but for other applications (e.g., those in which the number of precomputed images exceeds the amount of available memory or those in

R. W. Cohn is with the Department of Electrical Engineering, University of Louisville, Louisville, Kentucky 40292. M. Liang is with Neuristics Corporation, Baltimore, Maryland 21204-2316.

Received 9 June 1995; revised manuscript received 30 November 1995.

0003-6935/96/142488-11\$10.00/0

© 1996 Optical Society of America

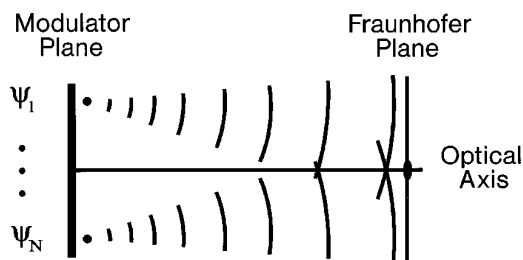


Fig. 1. Fraunhofer diffraction geometry illustrating superposition of a large number of wave fronts from independently phased, equal-intensity point sources.

which the desired full-complex function is not necessarily known in advance), it may only be possible to program the SLM by a real-time algorithm such as pseudorandom encoding.

Several devices can in principle produce a 2π phase-modulation range, but far fewer are available in practice. Parallel-aligned nematic liquid crystals (also referred to as birefringent liquid crystals) have been known to produce pure phase modulation for some time.³ However, such devices have become available only recently. These include devices from Hughes, Hamamatsu, and Meadowlark Optics. Only the optically addressed SLM from Hamamatsu has a 2π modulation range (according to their technical data sheet dated October 1993). Epson researchers have also demonstrated programmable kinoforms using a birefringent liquid-crystal television (LCTV) panel.⁴ However, the device is a custom-modified version of a commercially available twisted-nematic display, and this device is not available outside Epson. Using commercially available twisted-nematic LCTV's, several researchers have identified phase-mostly modulation characteristics.⁵⁻⁷ These are achieved by the proper selection and orientation of polarizers and/or wave plates. Most interesting is the eigenpolarization mode in which an elliptical polarization is transformed into an identical polarization independent of the voltage applied across the liquid crystal.⁶ Phase shifts of 195° and better than $\pm 4\%$ uniformity of amplitude were achieved for a panel from the In Focus model TVT6000 video projector. Soutar and Monroe identified a configuration that produces 2.5π of modulation for LCTV panels from an Epson E1020 video projector.⁷ However, Soutar and Lu later noted that the modulation characteristics can vary substantially across this device.⁸ The (phase-only) deformable mirror device produces phase shifts through the displacement of micromechanical pixels in a direction parallel to the optical axis.⁹ However, fully addressable devices with this type of pixel have not yet been successfully demonstrated.

In spite of the limited availability of 2π modulation it is still possible to experimentally demonstrate the method of pseudorandom encoding on current modulators and to produce diffraction patterns that are quite similar to those predicted for 2π modulators. For the TVT6000 LCTV, several nonideal properties

must be recognized and controlled. Most critical is that, because the SLM does not produce full 2π modulation, there is always a dc component of the modulated light that is focused onto the optical axis. In order to separate the dc peak from the designed diffraction pattern, we add a phase ramp to the desired modulation. As the SLM cannot produce all values between 0 and 2π , multiple harmonics in addition to the fundamental of the designed diffraction pattern are produced. Although use of a carrier frequency in practical systems leads to an undesirable reduction in the usable bandwidth of the SLM, for our purpose of demonstration, this condition is acceptable. Before presenting the results of the experimental demonstrations, we review the method of pseudorandom encoding and describe how the modulator is configured for the experiments.

2. Review of the Method

The encoding procedure is designed for SLM's composed of one- or two-dimensional arrays of pixels. However, the subsequent equations describing the procedure [in particular, Eqs. (4)–(6)] are presented only as a function of one spatial coordinate. This is done in part to simplify presentation, but more so to emphasize that the performance of the procedure depends directly on the total number of pixels. [The generalization to two dimensions simply requires the replacement of any spatial coordinate x or spatial frequency component f_x with the two-dimensional components (x, y) or (f_x, f_y) .] The encoding procedure can be applied to any array of arbitrarily positioned pixels, but in the experiments we considered only regularly spaced arrays. The pixels have identically shaped apertures. Each pixel has unity-amplitude transmittance and can produce any value of phase between 0 and 2π . For purposes of design the value of the phase of the i th pixel located at position x_i is assumed to be its statistical average:

$$\bar{\psi}_i = \langle \psi_i \rangle, \quad (1)$$

where $\langle \cdot \cdot \rangle$ represents the expected-value or ensemble-average operator. The value of the phase actually produced by the pixel is

$$\psi_i = \bar{\psi}_i + \delta\psi_i, \quad (2)$$

where $\delta\psi_i$ is an unbiased random-phase offset. The offset is selected from a prespecified random distribution. The distribution determines the design value of the effective amplitude produced by the pixel. The set of all uniform random distributions with spreads between 0 and 2π is especially convenient for this purpose. Amplitude control between unity and 0 is provided according to

$$\bar{a}_i = \langle \exp(j\delta\psi_i) \rangle = \text{sinc}\left(\frac{v_i}{2\pi}\right), \quad (3)$$

where v_i is the spread of the uniform distribution. Because the values of Eq. (3) are in the range

between zero and one, we always assume that the full-complex modulation is normalized so that its maximum amplitude is unity. (A maximum amplitude of less than one would reduce diffraction efficiency and increase noise.)

To summarize the algorithm, we set the design or effective complex modulation $(\bar{a}_i, \bar{\psi}_i)$ equal to the desired full-complex modulation. Equation (3) is inverted to solve for spread ν_i . A value of $\delta\psi_i$ is selected from a uniform unbiased distribution of spread ν_i by a random number generation routine. The random-phase offset is added to the design value of phase [see Eq. (2)] to produce the actual modulation $(1, \psi_i)$.

The complex transmittance produced by a phase-only SLM consisting of an array of N identical subapertures centered at positions x_i is

$$t(x) = \sum_{i=1}^N \exp(j\psi_i)r(x - x_i), \quad (4)$$

where $r(x)$ is a function defining the clear area of the subaperture. The effective complex transmittance resulting from encoding each pixel is likewise written

$$\bar{t}(x) = \sum_{i=1}^N \bar{a}_i \exp(j\bar{\psi}_i)r(x - x_i). \quad (5)$$

The quality of the diffraction patterns produced by pseudorandom encoding can be appreciated by consideration of the expression for the expected intensity of the diffraction pattern. It has been shown to be¹

$$\bar{I}(f_x) = |\bar{T}(f_x)|^2 + N(1 - \eta)R^2(f_x), \quad (6)$$

where f_x is the spatial frequency, $\bar{T}(f_x)$ and $R(f_x)$ are Fourier transforms of $\bar{t}(x)$ and $r(x)$, respectively, and the average intensity transmittance

$$\eta \equiv \frac{1}{N} \sum_{i=1}^N \bar{a}_i^2 \quad (7)$$

can be viewed as a type of diffraction efficiency, as we describe below.

Equation (6), the expected value of the intensity, is composed of two terms. The first term represents the specular component of the diffraction pattern (caused by the coherent superposition of wave fronts originating from the SLM). It is identical to the diffraction pattern of the desired full-complex modulation, i.e., the square magnitude of Eq. (5). The second term represents the diffuse component (or speckle pattern) that is due to the superposition of randomly phased wave fronts. Its spatial distribution is identical to the diffraction pattern from the aperture of a single pixel. Many diffraction patterns of interest are much more directional than the pattern of a diffuse scatter. This directionality gain

over the more nearly white background noise often makes it possible to produce a close approximation to the desired diffraction pattern.

The amount of noise, and thus the quality of the reconstruction, is largely understood in terms of the diffraction efficiency η . The diffraction efficiency indicates the fraction of energy that appears in the coherent portion of the diffraction pattern. Since phase-only modulation does not attenuate, the remaining fraction of the incident energy, $1 - \eta$, is diffracted into the incoherent speckle background. In Ref. 1 we interpreted ηN as an effective number of nonrandom phase-only pixels. Equation (6) shows that increasing the diffraction efficiency (or equivalently, the number of nonrandom pixels) reduces diffuse scatter and would thus be expected to produce more accurate designs. Another way of viewing the relation between the desired modulation and its pseudorandom encoding is that the more efficient a full-complex modulation is, the greater is its similarity to phase-only modulation.

An expression for the standard deviation of the intensity of the diffraction pattern is also presented in Ref. 1. It provides a precise statistical bound on the accuracy of the diffraction pattern at every point across f_x . Although the expression is not duplicated in this paper, it is used here to calculate error bars on plots of the designed intensity patterns. Although the effective number does not provide information as detailed as the standard deviation, it can be calculated with much lower computational overhead. Also it is well-enough correlated with the standard deviation that it can be used to gauge the quality of the diffraction pattern in real-time applications. Standard deviation, η , and N can be used together to define peak-to-background noise and the signal-to-noise ratio as was done in Ref. 1.

3. Experimental Configuration

The experiments are performed with two LCTV panels from the red channel of two different TVT6000 video projectors. Oscilloscope measurements show that, when black-and-white signals are applied to the video input, the signals from the red, green, and blue driver boards of the projector are essentially identical. One LCTV is electrically reconnected to the driver board for the red channel, and the other LCTV is connected to the driver board for the blue channel (as illustrated in Fig. 2). Each of the two panels is connected through its own cable extender that we fabricated from a 1-m, 23-conductor, flat-laminated cable from Parlex Corporation and two zero-insertion-force flexible-printed-circuit connectors from Amp Incorporated.

The green LCTV is left in the projector. This is used to preview visually the image exactly as it is displayed by the LCTV panels. This provides an especially simple way to verify that the LCTV's respond correctly to the applied image. In fact, when a RS-170 standard composite video is applied to the video input of the projector, we observe that

only 440 video lines and only $\sim 94\%$ of the viewable portion of each line is displayed by the projector. In terms of sending a 640×480 pixel digitized image in video format from our frame grabber (Dipix 360f with optional video-display board), only 600×440 pixels are displayed. Because the LCTV has 480×440 pixels, there is a 1:1 mapping from frame-grabber lines to LCTV lines and a 5:4 mapping between pixels on a line.

A second issue in the mapping of the digital pixels is the modulation transfer function of the display. Loudin noted that a single video line produces two lines of video on the projected image from the LCTV.¹⁰ We also observed this. We further note that the projected lines are roughly half the brightness possible. When two adjacent rows are turned on, one fully bright row is displayed, and there is a dim row to each side of the bright row. Apparently, the LCTV pixels cannot fully charge during the pixel time slot, and thus the sampling time (of the thin-film transistors) is extended to overlap with that of the adjacent lines. With projector sharpness set at minimum the effect is of roughly the same magnitude in both the horizontal and the vertical directions.

The optical apparatus used to produce and measure diffraction patterns is shown in Fig. 2. A collimated, nearly uniform-intensity laser beam of 632.8-nm wavelength and linear polarization illuminates the entrance port of the optical system. Standard optical components between the laser source and the entrance port are used to filter and expand the beam spatially, rotate the polarization, and control the intensity of the beam. The SLM consists of the components between the two quarter-wave plates. Light from the output of the second wave plate is focused with a 381-mm focal-length $f/5$ (Sorl F15/5) lens. The optical Fourier transform of the SLM is observed with a video microscope that consists of a Cohu 4915-2000 CCD video camera with an active imaging area of $6.4 \text{ mm} \times 4.8 \text{ mm}$, a C-mount 120-mm extension tube–microscope barrel,

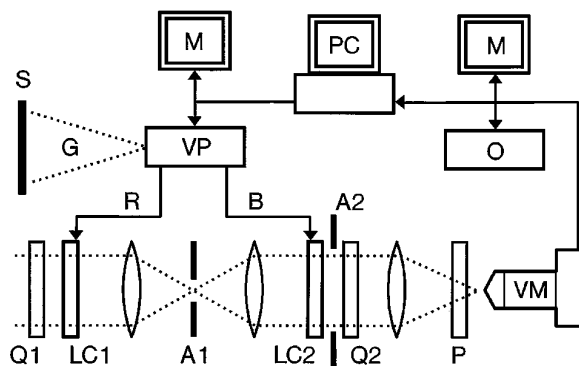


Fig. 2. Apparatus used for the experiments: VM, video microscope (or optical powermeter where noted in text); PC, personal computer that contains a frame grabber; VP, video projector; LC1 and LC2, LCTV's from the video projector; S, viewing screen; M, video monitor; O, digital oscilloscope; P, polarizer; A1 and A2, apertures; Q1 and Q2, quarter-wave plates.

and a microscope objective. The camera output is observed on a video monitor or captured with the frame grabber. The frame grabber is configured to acquire images simultaneously while continuously outputting a single image. Individual video lines are viewed with a digital oscilloscope (HP54503A) that has built-in video triggering.

A. Alignment of the Two LCTV's

The first LCTV (LC1) is imaged onto the second one (LC2) with a pair of 228.6-nm focal-length, $f/4.5$ imaging lenses (Plummer lenses purchased from MWK Industries). The second LCTV is rotated by 180° to account for the image inversion produced by the $4f$ imaging system. An Ealing adjustable rectangular aperture (A1) at the Fourier plane between the two lenses is set to pass only the signal information surrounding the central diffraction order of the LCTV grating–pixel pattern. The coordinates used to describe the polarizations are chosen so that x , or horizontal, is in the direction of the video scan line, y is in the vertical direction of the video, and z is opposite of the direction of laser propagation. Both LCTV's are oriented so that the laser light emerges from the side of the panels on which the electrical cable is visible. The first LCTV (LC1) is oriented so the cable is attached below the horizontal axis. In this coordinate system the first quarter-wave plate (Q1) is illuminated from a red helium–neon laser with a linear polarization of 70° from x and toward y . The fast axis of the first wave plate is at 45° , and the fast axis of the second quarter-wave plate (Q2) is at -45° . The polarizer (P) is oriented to pass light at 70° , the same as the incident linear polarization. The polarizer produces a substantial amount of wave-front distortion across its full aperture. The illuminated area and consequently distortion are reduced by placement of the polarizer near the focus of the Fourier-transform lens. The projector brightness and contrast controls are set to maximum, and the sharpness is set to minimum.

The effect of maximum sharpness is clearly evident on broadly extended diffraction patterns. In particular, if the LCTV is driven by a digital image of white noise, the envelope of the resulting speckle pattern resembles the diffraction pattern of a single pixel except that it is modulated in the horizontal direction by six high-contrast stripes covering the separation between adjacent diffraction orders of the SLM. This scallop-shaped pattern is reduced for the minimum sharpness setting. We further reduced the effect in our experiments by programming multiple adjacent pixels with the same video level, i.e., grouping pixels together into superpixels. The scalloped diffraction pattern is probably due to filtering produced from the combination of sharpness control, the LCTV pixel integration/charging time, and the 5:4 mapping between the frame grabber and the LCTV pixels.

Aperture A2 is chosen to be $15.2 \text{ mm} \times 15.2 \text{ mm}$. This limits the illuminated area of the SLM to 272

pixels by 332 lines. For the available lenses this permits registration of the image of the first LCTV onto the second LCTV to better than 0.5 pixel in both x and y . We verified the alignment by modifying the optics to make amplitude modulation evident. We did this by rotating the wave plates into an appropriate orientation and placing the polarizer and the video microscope immediately after the second LCTV. Aperture A1 at the Fourier plane between the two LCTV's is also opened so that the edges of individual pixel apertures from the first LCTV are observable through the pixel apertures on the second LCTV. Single-line and row-patterns are programmed onto the LCTV's, and micropositioners are used to align the patterns. The microscope is mounted on translation stages, and the alignment is checked at several positions across aperture A2. The alignment errors only become noticeable close to the edges of the aperture and appear to be caused by a slight barrel distortion in the imaging optics. After the alignment is set and/or tested in this way, aperture A1 is once again set to pass only the central diffraction order, and the system is reconfigured according to Fig. 2.

In addition to registration, aperture A2 is also needed in order to improve optical flatness so as to achieve near-diffraction-limited Fraunhofer patterns. We determined this by measuring the point-spread function of the SLM aperture with the video microscope. For the modulated light to be separated from the unmodulated light, the SLM, rather than being programmed with a constant gray-scale level, is programmed with a periodic ramp that displaces the point-spread function from the optical axis. (Details on selection of the ramp function and offset are given in Section 4.) Figure 3 compares the spread function measured at the focal plane of the transform lens with the diffraction pattern ideally produced by a 15.2-mm aperture and a 381-mm transform lens. The experimental intensity trace is taken across the center of the intensity peak, and it is aligned along a horizontal line of the camera in order to improve resolution. The correct scale for the spatial coordinates was determined by the manufacturer-quoted dimensions for the CCD imager to-

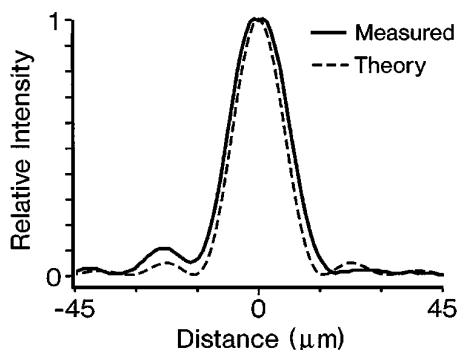


Fig. 3. Point-spread function of the SLM aperture as measured and predicted. The cross section is taken across the center of the spot perpendicular to the horizontal lines of the SLM.

gether with the measured magnification of 9.76X (nominally a 10 \times objective is used) for the video microscope.

B. Amplitude-Modulating Properties of the SLM

We also measured (using a photodetector and a powermeter in place of the video microscope) the variation in intensity of this central diffraction order when the uniform gray-scale image from the frame grabber is varied from full black to full white. The residual amplitude modulation is $\pm 3.7\%$ of the average amplitude modulation. The maximum transmittance is at a gray scale of ~ 128 , and there are two local minima at ~ 40 and ~ 256 .

We also measured energy utilization of the SLM between the input face of Q1 and the output face of Q2. We did this by measuring the intensity flux across the (effective) input and output apertures (A2 projected onto Q1 and Q2.) With the SLM set for maximum transmittance, only 0.325% of this incident energy is measured at Q2. Because one desirable feature of the eigenpolarization mode is its low loss, we were initially concerned about the low optical efficiency. We also configured the system as a phase-only modulator by illuminating each LCTV with a linear polarization and passing the linear polarization that most closely approached phase-only operation. The efficiency of this cascade is 1/6 that of the eigenpolarization arrangement. (It also has a similar phase-modulation range.)

The most significant loss factor is apparently related to the shadow mask in each LCTV panel. Measurements under a microscope indicate that the pixel aperture is roughly $28\ \mu\text{m} \times 28\ \mu\text{m}$ on a pitch of $56\ \mu\text{m}$ horizontally by $46\ \mu\text{m}$ vertically, leading to a fill factor of approximately 30%. Therefore only 30% of the energy is transmitted through the first shadow mask. Based on the Fourier-series analysis of a square wave, only 30% of this energy remains in the zero order at the filter plane between the two lenses of the imaging system. Owing to the spatial filtering of the nonzero orders, the second LCTV should produce an identical reduction in the transmitted flux. Overall, these losses would lead to a transmittance of 0.86%. Thus in this configuration even moderate fill factors can be the dominant source of loss.

C. Phase-Modulating Properties of the SLM

We initially measured the phase shift by building a Mach-Zehnder interferometer around the SLM arrangement shown in Fig. 2. The reference beam was tilted to produce fringes vertical to the video scan. The shift of the fringe between the row driven with gray scale 0 and a row driven with another value of gray scale was measured. These measurements indicate that the phase increases monotonically from 0° to 326° . A rough curve that approximately describes the phase shift as a function of gray scale is a curve that has a linear slope of 2° gray-

scale level between gray-scale levels 0 and 140 and 0.4° per gray-scale level between 140 and 255.

This measurement procedure, however, appears to be subject to several errors, including coherent noise, curvature, low contrast, and vibration (caused by air turbulence) of the fringes. Furthermore, we had concerns about errors introduced by the additional optical components of the interferometer. A second measurement procedure was devised in order to confirm the phase measurements. The procedure also indicates the dependence of the phase modulation on the spatial frequencies of the signal applied to the SLM. To perform the measurement, one loads a pseudorandom binary-level pattern into the frame grabber. An aperture and a powermeter are positioned at the focal plane of the transform lens shown in Fig. 2 so as to intercept the central diffraction order. Half the SLM pixels are randomly selected and driven with a gray-scale value of 0. The other half are driven with a second gray-scale value chosen between 0 and 255. The intensity measured on the powermeter is recorded as a function of gray scale. The measurement was repeated for various SLM pixel sizes, where an SLM pixel is defined to be an $n \times m$ array of LCTV pixels that are programmed with the same gray-scale value. These results are plotted in Fig. 4.

Diffraction from a binary-level, phase-only modulation can be understood by the analyses from Ref. 1 that were used originally to describe pseudorandom encoding. In this case each pixel is programmed to have an identical effective amplitude that produces an expected intensity pattern consisting of a diffraction-limited spot centered on the optical axis and a broad background noise level. Because the light from all SLM pixels mutually interferes at the intersection of the optical axis and the focal plane (i.e., f_x equal to zero), as illustrated in Fig. 1, the intensity of the spot depends directly on ψ , the difference between the two phases present on the SLM. The phasing on axis can be evaluated by deterministic analysis alone. For an ideal phase-

only SLM in which each pixel can be controlled independently of all others, the intensity of the diffraction peak on the optical axis is

$$I(0) = N^2 R^2(0) \frac{1 + \cos \psi}{2}, \quad (8)$$

where N is the number of SLM pixels and $R(f_x)$ (introduced in Section 2) is the element factor corresponding to the pixel-clear aperture. As would be expected, Eq. (8) indicates that there is perfect cancellation of the spot for a phase difference of 180° . (In practical measurements a finite detector size and nearby speckles would introduce errors into the measurement of power. However, because N is usually a large number, speckle noise is not a serious source of error over most of the phase range. Assuming that the SLM has adequate phase range, it would also be possible to offset the lower gray-scale value from zero to a larger value in order to more clearly measure the 180° point.)

Based on the initial phase measurements with the Mach-Zehnder interferometer, it is reasonable to expect that there would be a simple and direct relation between the phase difference and the non-zero gray-scale value. Indeed, the curves in Fig. 4 show a qualitative agreement with this model in that they resemble a cosine function for gray-scale values of <128 . For gray-scale values of >128 the intensity increases but much more slowly than for the lower gray-scale values. This tracks with the interferometer measurements of phase in which the phase sensitivity to gray scale decreased at large values of gray scale.

The curves indicate that the phase-modulation range increases with SLM pixel size. The maximum range in these curves is for the 12×12 array. The maximum value of $I(0)$ after the phase exceeds 180° is 0.57. Inverting Eq. (8) gives an estimated modulation range of 278° . For the 4×1 SLM pixel there is barely a 180° range. The correspondence with the original interferometer measurements appears to be good for low spatial frequency patterns of modulation; however, the actual phase modulations needed for the encoding experiments have a range of frequencies from high to low.

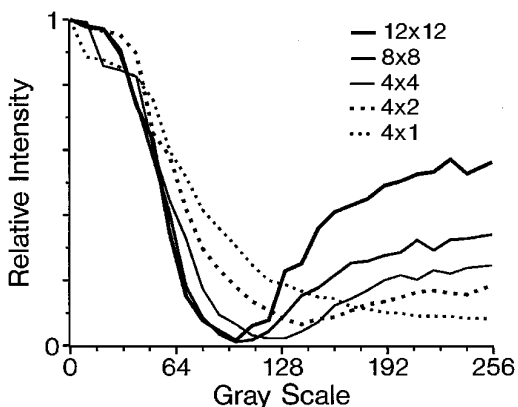


Fig. 4. On-axis diffraction intensity for random binary gray-scale patterns and with superpixels of various sizes. Each curve is normalized to the peak intensity with the gray scale equal to zero.

D. Summary of SLM Properties

The cascade of two SLM's was originally intended to produce a phase modulator with a range of 360° . The measured SLM does have a small degree of residual amplitude modulation. It also has a large phase-modulation range that is close to 360° but only for modulations with low spatial frequencies. The phase-modulating characteristics can be made independent of spatial frequency by use of large SLM pixels; however, this significantly reduces the number of available pixels for the encoding experiments. (For the case of 12×12 SLM pixels and the available clear aperture there are fewer than a thousand individual pixels.)

4. Experimental Demonstrations of Pseudorandom Encoding

A. Adjustments Made for Demonstrations with the Available SLM

Because the available SLM does not achieve a 360° range, there is usually a dc component in the spatial modulation and a corresponding diffraction peak at f_x equal to zero. We chose to separate the dc component by multiplying the modulation by a periodic function. We accomplish this by adding together a linear ramp function with the gray-scale values of the encoded signal, then removing integer factors of 256 by using the module base-256 function, and placing this image in the display memory of the frame grabber. Several harmonically related diffraction patterns are generated, of which the fundamental is usually the brightest. It is this fundamental diffraction pattern that we compare with those anticipated from our presumed phase-only modulator.

The fundamental spatial frequency of the phase ramp (i.e., the carrier frequency) also affects the quality of the diffraction pattern. This is most evident in that the point-spread function decreases with increasing phase ramp or carrier frequency. This is illustrated in Fig. 5, in which diffraction efficiency is plotted against the period of the carrier. Efficiency for this measurement is defined as the peak intensity normalized by the intensity of the spread function when it is centered on the optical axis (specifically, when all pixels of the SLM are programmed to gray-scale value 0). The peak intensities are measured (with the digital oscilloscope from Fig. 2) across a single video line of the CCD camera (rotated 90° from horizontal lines of the SLM). Figure 5 can be viewed as a type of modulation transfer function. The curve shows, for periods between 20 and 70 SLM lines, that the diffraction efficiency is close to flat. The efficiency falls off rapidly at <10 lines. For the pseudorandom-encoding demonstrations, presented below, a period of 20 lines was found to be acceptable. As the period increases to >20 lines, interference from

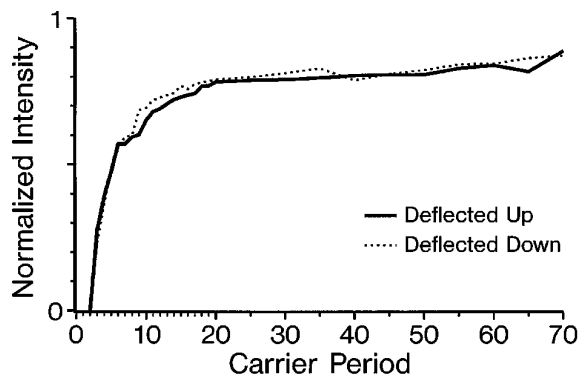


Fig. 5. Intensity of the deflected point-spread function as a function of the carrier period. Intensities are normalized to the intensity of the undeflected (on-axis) point-spread function. The unit for the carrier period is the number of horizontal SLM lines per period.

overlap with the dc and the first-harmonic order becomes increasingly significant. Figure 5 (and also Fig. 4) indicates that individual pixels are not independent of the modulation of nearby pixels. It is surprising that there is still residual correlation between pixels that are 10 and 20 lines apart. Certainly, by any criteria, the resolution of the SLM is far worse than one pixel.

The various issues relating to making the SLM behave as an array of independently controllable pixels cannot be well satisfied with the given constraints of maintaining a diffraction-limited aperture, the low spatial resolution of the SLM, the lack of 1:1 mapping between display board pixels and SLM pixels along the scan line, and the need for a large number of pixels. These constraints led us to program the SLM as clusters of superpixels. Each superpixel consists of 4 pixels along a single scan line for 22,000 total pixels, which is roughly the same number of pixels (16,384) as used in the simulations in Ref. 1. Using a 4×2 superpixel was not considered after noting, based on Fig. 4, that the total phase-modulation range would increase to only 193° , an increase of as little as 13° . Thus the SLM is programmed as if it consists of 68×332 superpixels, and the carrier has a period of 20 lines in the vertical direction.

B. Design and Encoding of Full-Complex Modulations for Beam Shaping

Three apodizations are designed to produce rectangularly shaped diffraction patterns centered on the optical axis. The apodization is the product of a sinc function and a Dolph window in the x , or horizontal, direction.¹¹ This window is chosen to reduce the Gibbs ripple that can result from the finite extent of the SLM truncating the sinc function. The specific Dolph function selected is defined by the sidelobe level of its Fourier transform $d(f_x)$, which for these designs is 26 dB. Higher-sidelobe-level Dolphs are known to further reduce the Gibbs ripple, but they also increase transition bandwidth. As for pseudorandom encoding, higher-sidelobe-level Dolphs are more steeply tapered, which reduces the value of diffraction efficiency η [see Eq. (7)] and consequently increases the speckle noise [see Eq. (6)]. In the computer simulations of random-encoding-designed diffraction patterns in Ref. 1, a 26-dB sidelobe level was empirically found to provide a good trade-off between reduction in the Gibbs ripple and background noise. The same apodization was applied both in the horizontal and the vertical directions. In the designs for the experiments presented here, the apodizations vary in only the vertical direction. The one-dimensional apodization is used with the objective of further increasing the diffraction efficiency and reducing the random noise inherent to the encoding procedure. The apodizations are chosen to produce diffraction-intensity patterns of the form

$$I(f_x, f_y) \propto \text{sinc}^2(f_x) [d(f_y) * \text{rect}(f_y/w)]^2, \quad (9)$$

where $\text{sinc}^2(f_x)$ is the point-spread function in the x direction and $d(f_x)$ is the Fourier transform of the Dolph window. The amplitude in the y direction is designed to approximate a rect function of width w for values of 2, 3, and 4. The width is normalized in terms of the unity width (from peak to first null) of $\text{sinc}^2(f_y)$, the point-spread function in the y direction. From Fig. 3 it can be seen that $w = 1$ corresponds to a physical distance of $\sim 15 \mu\text{m}$.

Each of the three apodizations are pseudorandomly encoded by Eqs. (1)–(3). As described above, these modulations are then multiplied by a carrier frequency with a period of 20 video lines before they are loaded onto the frame grabber. Theoretical diffraction patterns of the apodizations are also calculated. This is done with a 256×4096 array fast Fourier transform on the 68×332 array designed modulations (zero padded to the size of the fast-Fourier-transform array). Cross sections in the y direction from the centers of the theoretical diffraction patterns are saved for comparison with the measured diffraction patterns.

C. Summary of Experiments and Their Comparisons with Theory

The diffraction patterns are recorded with the CCD camera in the video microscope rotated by 90° from the x (horizontal) and the y coordinates of the SLM. The resulting images are shown in Fig. 6. In each of the four images the CCD camera is saturated by roughly the same factor with respect to the peak intensity of the desired pattern in order to aid in comparisons of the background levels. Figure 6(a) is the image of the point-spread function. (The cross

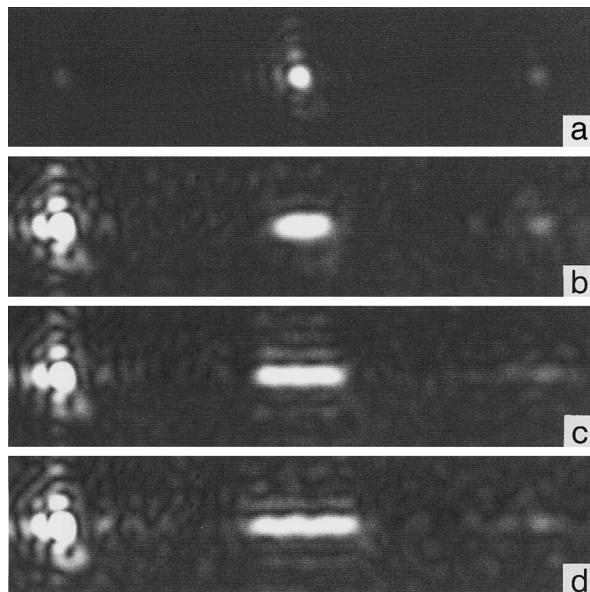


Fig. 6. Gray-scale images of the measured diffraction-pattern intensity: (a) the measured point-spread function (cross section shown in Fig. 3). The measured diffraction patterns that are designed to approximate a rect function in f_y are of widths (b) $w = 2$, (c) $w = 3$, and (d) $w = 4$. The images are oriented so that f_y is horizontal to the page.

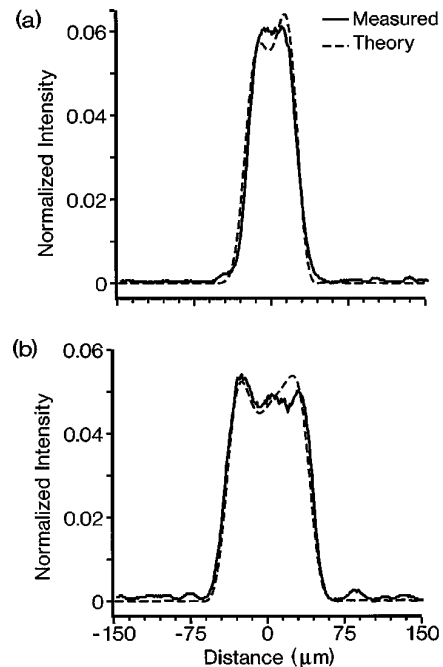


Fig. 7. Theoretical and measured diffraction patterns. Measured intensity curves are normalized with respect to the peak intensity of the measured point-spread function in Fig. 3. Cross sections are taken from the centers of the diffraction patterns shown in (a) Fig. 6(b) and (b) Fig. 6(c). Theoretical intensity plots are scaled by $1.96\times$ in (a) and by $1.53\times$ in (b) with respect to the peak intensity of the theoretical point-spread function from Fig. 3. Both measured curves are plotted with a $+4\text{-}\mu\text{m}$ offset from the center of the measured point-spread function.

section of this diffraction pattern is shown in Fig. 3.) The cross sections corresponding to Figs. 6(b)–6(d) are shown in Figs. 7 and 8(a). Except for changes in attenuator settings, the corresponding curves and images were recorded under identical conditions and within a few minutes of each other.

Figure 6(a) shows that a substantial amount of energy is deflected into the fundamental order and that there is much less energy at dc and the first harmonic. The first diffraction order (not shown) to the left of dc is much weaker than the fundamental but stronger than dc and the first harmonic. Figures 6(b)–6(d) show the successive widening of the beam footprint. The first harmonic is still quite faint for the shaped beams, but dc is now very bright. As can be seen from the vertical axes in Figs. 7 and 8(a), the intensity of the fundamental is much less than it is in Fig. 6(a). The sidelobe structure of the dc component in Figs. 6(b)–6(d), although more heavily saturated, closely resembles the point-spread function in Fig. 6(a). Each of these diffraction patterns also shows, as expected, both a background speckle pattern and sidelobes along the narrow direction of the beam footprint.

Figures 7 and 8(a) provide more precise information describing the measured diffraction patterns. The three measured curves are normalized to the peak intensity of the experimental point-spread function in Fig. (3). The three theoretical curves were

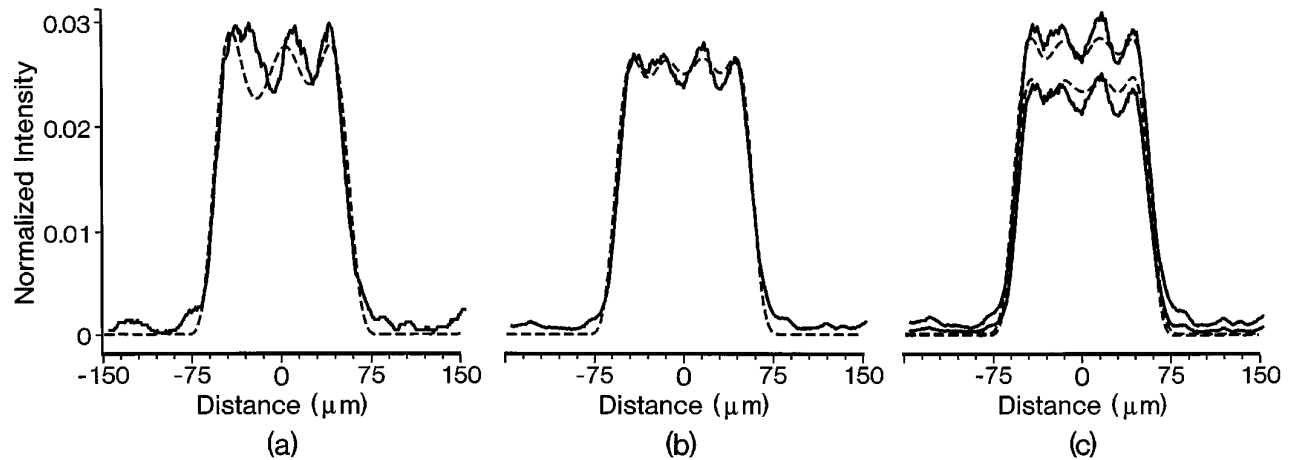


Fig. 8. Theoretical (dashed curves) and measured (solid curves) diffraction patterns: (a) cross section of the center of the diffraction pattern shown in Fig. 6(d); (b) the average of 120 cross sections with a different random seed for each experiment; (c) the error bars (plus and minus one standard deviation) of the average intensity in (b). Curves are normalized the same as in Fig. 7 except that the measured curves are plotted with a +5- μm offset, and the theoretical curves are scaled in intensity by a factor of 1.64 \times .

initially normalized by the peak intensity of the theoretical curve in Fig. 3, but the curves were found to be somewhat lower than the experimental intensities. Multiplying the theoretical curves by vertical scale factors (between 1.53 and 1.96 as noted in the corresponding figure captions) helps to show just how similar the curves are in shape. Offsetting the measured data by 4–5 μm further improves the correspondence, but to a much lesser degree. In these experiments the scale-factor difference between experiment and theory is the most significant discrepancy. The offset in position is rather small when compared with the diameter of the point-spread function. These discrepancies are probably due to one or more of the nonideal properties of the actual SLM, none of which were factored into our theoretical model. It is not our goal to account for these differences quantitatively but rather to gain insight into how the encoding method would behave when 360° modulators become available. For this reason we think that the degree of correspondence, while qualitative, is nonetheless excellent, and we are encouraged by this result.

Further evidence of the correspondence between experiment and theory can be demonstrated by repeated trials of the pseudorandom-encoding procedure. An example of this is given in Fig. 8. Here, the experiment leading to the result in Fig. 8(a) is repeated 120 times. The only difference between each trial is that the random-number generator is initiated with a different random seed for each encoding. The average intensity of the 120 trials (both experiment and theory) is calculated, as are the plus and minus one standard-deviation error bars of the intensity pattern. The number of trials is adequate to produce theoretical diffraction patterns that, for purposes of plotting, are nearly identical to the ensemble average that would be found for an infinite number of trials [i.e., found by Eq. (6) and the equation for standard deviation in Ref. 1]. One can

appreciate the small difference by noting that the theoretical curve in Fig. 8(b) has almost equal-level ripples, whereas the expected intensity for an infinite number of trials has exactly equal-level ripples. This degree of agreement between theory for a finite and theory for an infinite number of trials was found for the theoretical results in Fig. 8(c) as well.

The measured and the theoretical average curves in Fig. 8(b) show more clearly the correspondence than does Fig. 8(a). The discrepancies between the two average curves indicate differences caused by systematic errors in the experiment.¹² Most notably, the measured curve exhibits more ripple and higher sidelobes, or noise. The larger error bounds in Fig. 8(c) indicate that more random noise is being introduced into the measurement than that for the theory (in which noise is due only to the random statistics used in encoding). The measured error bounds are only ~60% wider than those for theory in band. Nonetheless, we think that the degree of agreement is quite good considering that the SLM is so different from the assumed device, a 360° phase-only SLM. Most important is that the diffraction patterns produced do qualitatively agree with our theory in that the beam shape is controllable and there is a broad, near-uniform intensity speckle background. As devices that do produce 360° become available, it appears that it will be possible to synthesize diffraction patterns with greatly improved accuracies. Elimination of the need for a carrier frequency will also make it possible to use the entire bandwidth of the SLM for signal processing.

5. Summary and Conclusions

A. SLM Measurements and Characterization Procedures

A secondary goal of this paper has been to describe the properties of the SLM and how they were measured. In most previous studies of electrically addressable SLM's, the modulation transfer function

has been ignored. Our measurements, in which we applied different carrier frequencies, indicate that spatial frequencies of <5 SLM lines are substantially filtered. There is even a nontrivial amount of filtering at 10–15 SLM lines. The filtering reduces the phase-modulation range and causes the random-phase components at nearby pixels to become statistically correlated. This point may have been overlooked in some previous interferometric studies of SLM phase-modulating properties in which large blocks of pixels were programmed with the same gray-scale value.

Recently, two groups have focused on common-path interferometric approaches in order to eliminate vibrations.^{13,14} One procedure is as follows: (1) the beam is split with a Ronchi ruling; (2) one beam is passed through a reference portion of the SLM (programmed to gray scale 0), and the second beam is passed through a portion of the SLM that is modulated with a second gray-scale value; (3) the beams are recombined and detected by camera; and (4) the phase shift of the sinusoidal interference pattern is measured.¹³ The second procedure is as follows: (1) a 50% duty-cycle square wave (Ronchi ruling) is programmed onto the SLM with half the gray-scale values set to 0 and the other half set to a second level; (2) the diffraction pattern of the SLM is detected by camera; and (3) the phase is decoded based on the relative intensities of the first and the third diffraction orders.¹⁴ An alternative common-path procedure is described here in which a pseudo-random binary-phase-modulation pattern is applied to the device. The method is useful in that it is an *in situ* measurement procedure that requires no extra beam splitters or combiners, and various-sized superpixels can be evaluated. Because only the intensity of the on-axis diffraction pattern is needed, the measurement can be performed with a single photodetector. Also, over most of the phase range, the diffraction-limited spot is much brighter than the background speckle noise, which can lead to repeatable measurements of phase. For SLM's that have fairly uniform characteristics across the surface of the device and for which the amplitude variation is also known, it will also be possible to measure the phase with high precision.

B. Experimental Demonstration of Pseudorandom Encoding

We attempted to develop a 360° modulator by cascading two TVT6000 SLM's. A modulation range of 326° was measured initially. However, the phase modulation was also found to depend on the spatial frequencies present on the SLM. For high spatial frequencies the modulation range decreases to $\sim 180^\circ$. Although it was found that increasing the size of superpixels also increases the phase-modulating range, the superpixels could not be made large enough to simultaneously eliminate the sensitivity of the SLM to spatial frequencies and provide a reasonably large number of pixels for the encoding

experiments. It is comforting to note that the carrier frequency and the apodization are slowly varying functions. However, the random-phasing portion [see Eq. (2)] of the modulation pattern (that controls amplitude) contains the highest spatial frequencies. The portions of the apodization that are designed to produce the smallest amplitudes will have the largest random spread [see Eq. (3)] and thus the most rapid phase transitions between adjacent pixels. Thus the low-amplitude portions are expected to be the most in error owing to the modulation-transfer-function limitations of the SLM. In addition, the nonlinear mapping between gray scale and phase was not factored into the theoretical diffraction pattern. The use of the carrier frequency also means that different portions of the apodization pattern are phase encoded by different ranges of the nonlinear mapping curve. Despite these properties, which are significantly different from an ideal array of independent 360° phase-only pixels, qualitatively similar results were produced. Not only were the diffraction patterns very similar in shape to ideal, but a broad background of speckle was observed. The statistically averaged experimental results were also quite similar to theory, and the error bounds were only somewhat noisier than theory. These experimental results lead us to conclude that pseudo-random encoding is a robust procedure in that the theoretical predictions will reasonably match the experimental results without use of a perfectly ideal SLM.

This research is sponsored by Advanced Research Projects Agency through Rome Laboratory contract F19628-92-K0021, U.S. Army Research Office contract DAAH04-93-G-0467, and National Aeronautics and Space Administration cooperative agreement NCCW-60 through Western Kentucky University.

References

1. R. W. Cohn and M. Liang, "Approximating fully complex spatial modulation with pseudo-random phase-only modulation," *Appl. Opt.* **33**, 4406–4415 (1994).
2. J. L. Horner and P. D. Gianino, "Phase-only matched filtering," *Appl. Opt.* **23**, 812–816 (1984).
3. N. Konforti, E. Marom, and S.-T. Wu, "Phase-only modulation with twisted nematic liquid-crystal spatial light modulators," *Opt. Lett.* **13**, 251–253 (1988).
4. J. Amako and T. Sonehara, "Kinoform using an electrically controlled birefringent liquid-crystal spatial light modulator," *Appl. Opt.* **30**, 4622–4628 (1991).
5. K. Lu and B. E. A. Saleh, "Theory and design of the liquid crystal TV as an optical spatial phase modulator," *Opt. Eng.* **29**, 241–246 (1990).
6. J. L. Pezzaniti and R. A. Chipman, "Phase-only modulation of twisted nematic liquid-crystal TV by use of the eigenpolarization states," *Opt. Eng.* **18**, 1567–1569 (1993).
7. C. Soutar and S. E. Monroe, Jr., "Selection of operating curves of twisted-nematic liquid crystal televisions," in *Advances in Optical Information Processing VI*, D. R. Pape, ed., *Proc. SPIE* **2240**, 280–291 (1994).

8. C. Soutar and K. Lu, "Determination of the physical properties of arbitrary twisted-nematic liquid crystal cell," *Opt. Eng.* **33**, 2704–2712 (1994).
9. R. M. Boysel, J. M. Florence, and W. R. Wu, "Deformable mirror light modulators for image processing," in *Optical Information Processing Systems and Architectures*, B. Javidi, ed., Proc. SPIE **1151**, 183–194 (1989).
10. J. A. Loudin, "LCTV custom drive circuit," in *Optical Pattern Recognition V*, D. P. Casasent and T. H. Chao, eds., Proc. SPIE **2237**, 80–84 (1994).
11. F. J. Harris, "On the use of windows for harmonic analysis with the discrete Fourier transform," *Proc. IEEE* **66**, 51–83 (1978).
12. R. W. Cohn and J. L. Horner, "Effects of systematic phase errors on phase-only correlation," *Appl. Opt.* **33**, 5432–5439 (1994).
13. C. Soutar, S. E. Monroe, Jr., and J. Knopp, "Measurement of the complex transmittance of the Epson liquid crystal television," *Opt. Eng.* **33**, 1061–1068 (1994).
14. Z. Zhang, G. Lu, and F. T. S. Yu, "Simple method for measuring phase modulation in liquid crystal televisions," *Opt. Eng.* **33**, 3018–3022 (1994).